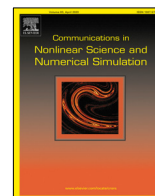




Contents lists available at ScienceDirect

# Communications in Nonlinear Science and Numerical Simulation

journal homepage: [www.elsevier.com/locate/cnsns](http://www.elsevier.com/locate/cnsns)

Research paper

## A numerical method for two-phase flow with its application to the Kelvin–Helmholtz instability problem

Abdullah Shah <sup>a,\*</sup>, Muhammad Sohaib <sup>a,b,c</sup>, Li Yuan <sup>d,e</sup><sup>a</sup> Department of Mathematics, King Fahd University of Petroleum and Minerals, 31261, Dhahran, Saudi Arabia<sup>b</sup> Department of Mathematics, COMSATS University Islamabad, Park Road, Islamabad 45550, Pakistan<sup>c</sup> Department of Mathematics and Statistics, Bacha Khan University, Charsadda 24461, Pakistan<sup>d</sup> LSEC and NCMIS, Institute of Computational Mathematics, Academy of Mathematics & Systems Science, Chinese Academy of Sciences, Beijing 100190, PR China<sup>e</sup> School of Mathematical Sciences, University of Chinese Academy of Sciences, Beijing 00190, PR China

### ARTICLE INFO

#### Article history:

Received 12 October 2022

Received in revised form 21 March 2023

Accepted 28 May 2023

Available online 2 June 2023

#### Keywords:

Kelvin–Helmholtz (KH) instability

Allen–Cahn Navier–Stokes model

Artificial compressibility

WENO scheme

Dual time–stepping

ADI scheme

### ABSTRACT

This article uses the artificial compressibility-based high-order finite difference method to simulate the two-phase Kelvin–Helmholtz (KH) instability problem. The equations are based on the mass-conserving Allen–Cahn equation coupled with the incompressible Navier–Stokes equations. One of the advantages of the artificial compressibility approach is that many high-order numerical schemes based on hyperbolic conservation law can be applied. A fifth-order weighted essentially non-oscillatory (WENO) scheme is used for discretizing the convective terms while a standard central finite difference scheme is used for the viscous and surface tension terms. The system of equations is then solved using the Beam–Warming approximate factorization technique. For validation, the effects of both single- and double-mode sinusoidal perturbations on the Kelvin–Helmholtz instability dynamics are analyzed. When there is a single-mode sinusoidal perturbation, the interface roll-up at the center of the domain. Additionally, the role of the surface tension parameter in the instability's dynamics is investigated. The development of Kelvin–Helmholtz instability is shown to be sensitive to the surface tension value. The analysis of grid convergence is also performed to capture the interface dynamics at varying resolutions. The comparison of the computed results is in good agreement with those from the literature. It is observed that the proposed technique effectively resolves the dynamics of the chaotically distorted interfaces of the Kelvin–Helmholtz instability in two-phase flow.

© 2023 Elsevier B.V. All rights reserved.

## 1. Introduction

When there is a substantial velocity/density difference between two immiscible fluids, a phenomenon known as the Kelvin–Helmholtz (KH) instability arises. Because of the gravity and surface tension, the interface for which the lighter fluid is on top of the heavier fluid remains stable. However, the KH instability arises when the destabilizing effects of the shear surpass the stabilizing effects of the gravity or surface tension. The KH instabilities may be seen in a variety of different natural settings. In the lower atmosphere, billowing clouds are a well-known manifestation of KH instability. Kelvin [1] and Helmholtz [2] are credited for conducting the initial work on this instability. Different techniques, including

\* Corresponding author.

E-mail address: [abdullah.shah.1@kfupm.edu.sa](mailto:abdullah.shah.1@kfupm.edu.sa) (A. Shah).

analytical [3], experimental [4], and numerical [5–8], have been used to analyze the linear and nonlinear stabilities of the KH instability.

Funada and Joseph [9] used the viscous potential flow analysis to investigate the Kelvin–Helmholtz instability in a channel. They performed an analysis of the planar interface without taking into account heat and mass transport. Funada and Joseph [10] tested the validity of the theory of viscous potential flow by comparing the fully viscous flow theory for a stationary cylindrical liquid with the capillary instability criterion suggested by the theory of viscous potential flow. The exact normal mode solution of the linearized Navier–Stokes equations is found in the fully viscous flow theory. With varying Reynolds numbers, they determined the instability growth rates. The linear Kelvin–Helmholtz instability of the interface between two viscous and incompressible fluids was investigated by applying the Viscous Correction of the Viscous Potential Flow (VCVPF) theory developed by Joseph and Wang [11] when the phases are enclosed between two horizontal cylindrical surfaces coaxial with the interface and mass and heat transfer across the interface are present [12].

Shadloo and Yildiz [13] used the smoothed particle hydrodynamics method to explore numerically the dynamics of the two-phase incompressible KH instability. They have shown that the Richardson number is the key factor in determining how fast the KH instability develops. By using the lattice Boltzmann multi-phase model, Zhang et al. [14] examined the impact of surface tension on the dynamics of the interface between two immiscible fluids. When the surface tension is high, formation of many pinch-offs at the interface and tiny droplets are observed. Atmakidis and Kenig [15] examined the unstable wavy structures (viscous fingering and roll-ups etc.) of the interface using the Level Set and Volume of Fluid approaches. The disappearance of the finger-like shape was noted as a result of larger surface tension. Shin et al. [16] analyzed the long-time behavior of the KH instability using the vortex sheet model. They have studied the rolling of the interface by varying the density ratio. When the KH instability is simulated over a long period of time using an adaptive vortex approach, Sohn et al. [17] found that the internal roll-up is distorted and the KH instability finally develops into a disordered structure and a secondary instability is formed. Using the front tracking method, Tauber et al. [18] found that the interface between two sheared immiscible fluids takes on a finger-like structure at high Reynolds and low Weber numbers. By using the vortex-sheet approach, Rangel and Sirignano [19] numerically investigated an initially perturbed interface and examined the impact of both surface tension and density ratio. By increasing the surface tension or density ratio, they observed, the disturbance could be slowed down. Pressure-driven displacement flow in an immiscible two-fluid system was analyzed in two [20] and three [21] dimensions by Redapangu et al. using the multiphase lattice Boltzmann technique. They concluded that, on average, the flow is more uniform in a three-dimensional channel than in a two-dimensional channel, and that screw-type instabilities are more easily noticed in the former. Cenicerros and Roma [22] used the immersed boundary method to simulate the long-term development of a sheared two-phase immiscible fluid system with the same density and viscosity.

The problem of interfacial dynamics in multi-phase flows is associated with several industrial applications. In recent years, several numerical techniques are competing for multi-phase flows. The moving interface problems, in which the interface acts as a discontinuity separating one fluid from the other, is also known as the moving boundary problems. The tracking of moving interface is a challenging task both theoretically and numerically. One type of moving interface method is characterized as a sharp interface, while the other types are described as a phase-field or diffuse interface method. In contrast to the phase-field method, where the interface is taken with a nonzero finite thickness, the sharp interface method assumes that the interface has a zero thickness [22]. For multi-phase flows, the phase-field method is getting attention more and more due to its several computational advantages over the sharp interface method such as the interface can be updated as part of the numerical solution without any re-initialization as in the case of the level-set method or complicated geometry as in the VOF method [15]. Also, it is a physically consistent approach that is based on the minimization of the free energy functional. The governing equations for the two-phase flow are the Navier–Stokes equations coupled with the nonlinear Cahn–Hilliard [23] or the Allen–Cahn equations.

The objective of the current study is to simulate the KH instability problem using a high-order finite difference method which applies the artificial compressibility method to the mass-conserving Allen–Cahn equation and the incompressible Navier–Stokes equations [24]. Unlike the projection-type methods in which the velocity field and pressure are decoupled, the current method solves the governing equations implicitly in a coupled way by recasting the original equations into a conservative form. With the artificial compressibility approach, the dual time-stepping technique [25] is used for time discretization in which physical time is discretized with a second-order accurate backward formula whereas the pseudo-time is discretized with the forward difference formula. The spatial part is discretized using the finite difference method whereas the convective term is discretized using the fifth-order WENO scheme [26] and viscous terms by the standard fourth-order central difference scheme.

The main advantage of the artificial compressibility approach is the ease of using many high-order numerical schemes developed for hyperbolic conservation laws so that the Kelvin–Helmholtz problem can be investigated with high resolution and without generating spurious numerical oscillations. Since the AC method is widely used in the numerical simulation of incompressible flows in engineering, it is interesting to see if it works fine for the combined phase field model and the INS equations [27]. Since KH instability is often encountered in atmospheric and oceanic sciences, geophysics, and engineering, this study may be useful in such areas of research. When compared to the fourth-order Cahn–Hilliard equation, the discretization of the Allen–Cahn equation is straightforward because only the second-order derivative term is present. A significant drawback of the Allen–Cahn equation is that it is not mass-conservative. However, the Lagrange multiplier has been included in our studies to circumvent the mass loss at each physical time step, allowing for the mass-conserving simulation of the KH instability problem.

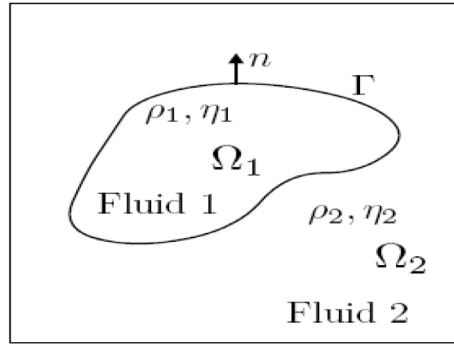


Fig. 1. Schematic diagram of a two-phase flow domain.

The paper is structured as follows: In Section 2, we provide the physical assumptions and the governing equations that the flow of two incompressible immiscible fluids. The KH instability of a two-fluid system is described in detail in Section 3. The numerical scheme is elaborated in Section 4. The numerical experiments are carried out in Section 5. The conclusion is given in Section 6.

### 2. Allen-Cahn Navier–Stokes model for mixture of two immiscible fluids

Consider a two-dimensional domain  $\Omega = \Omega_1 \cup \Omega_2 \subseteq \mathbb{R}^2$  filled with two different fluids having density and viscosity  $\rho_1, \mu_1, \rho_2$ , and  $\mu_2$  respectively as Fig. 1. By introducing a smooth but nearly piece-wise function  $\phi(\mathbf{x}, t) = \pm 1$  to label the two fluids e.g.,  $\phi(\mathbf{x}, t) = +1$  in one fluid and  $\phi(\mathbf{x}, t) = -1$  in the other with  $\phi(\mathbf{x}, t) = 0$  as the interface. In the phase-field model, the two fluids are separated by a thin transitional layer of thickness  $0 < \epsilon \ll 1$  so that the interface can be represented by  $\phi(\mathbf{x}, t) = \tanh(\mathbf{x}, t)/\epsilon$  as given below:

$$\phi(\mathbf{x}, t) = \begin{cases} -1, & \text{Fluid 1} \\ 1, & \text{Fluid 2} \end{cases} \approx \tanh\left(\frac{\mathbf{x}}{\epsilon}\right). \tag{2.1}$$

An expression for the free energy of a system with two fluids is as follows:

$$\mathcal{E} = \int_{\Omega} \left( \mathcal{F}(\phi) + \frac{1}{2} |\nabla\phi|^2 \right) dx, \tag{2.2}$$

where

$$\mathcal{F}(\phi) = \frac{1}{4\epsilon^2} (\phi^2 - 1)^2, \tag{2.3}$$

is the double well potential function.

Using the variational derivative with respect to the phase-field variable, we can determine the time evolution of the convective Allen–Cahn equation, which is given by

$$\phi_t + \mathbf{U} \cdot \nabla\phi = -\gamma \frac{\delta\mathcal{E}}{\delta\phi} = \gamma (\Delta\phi - \mathcal{F}'(\phi)). \tag{2.4}$$

In Eq. (2.4),  $\frac{\delta\mathcal{E}}{\delta\phi}$  denotes the variational derivative of the free energy,  $\mathcal{F}'(\phi) = \phi^3 - \phi$  and  $\gamma$  is the elastic relaxation time. By coupling the Allen–Cahn equation with the incompressible Navier–Stokes equations through velocity and surface tension, the dynamics of the two fluid system is examined with the following system [28]:

$$\rho [\mathbf{U}_t + (\mathbf{U} \cdot \nabla) \mathbf{U}] = -\nabla p + \nabla \cdot [\nu (\nabla\mathbf{U} + (\nabla\mathbf{U})^T)] + \nabla \cdot \mathbf{S}(\phi), \tag{2.5a}$$

$$\nabla \cdot \mathbf{U} = 0, \tag{2.5b}$$

$$\phi_t + \mathbf{U} \cdot \nabla\phi = \gamma (\Delta\phi - \mathcal{F}'(\phi)). \tag{2.5c}$$

In system (2.5),  $\mathbf{U}$  is the velocity-field,  $p$  is the pressure,  $\mathbf{S}(\phi) = -\lambda \nabla\phi \otimes \nabla\phi$  is the surface tension force, and  $\rho, \nu$  are the density and kinematic viscosity respectively. Since

$$\nabla \cdot \mathbf{S}(\phi) = -\lambda \Delta\phi \nabla\phi - \nabla \left( \frac{\lambda}{2} |\nabla\phi|^2 \right). \tag{2.6}$$

Combining the last term in Eq. (2.6) with the pressure term in Eq. (2.5), we obtained the modified pressure  $P = p + \frac{\lambda}{2} |\nabla\phi|^2$  by simplifying the momentum equation. We employed the same density and viscosity for both fluids in the current study i.e.,  $\rho_1 = \rho_2 = \rho, \nu_1 = \nu_2 = \nu$ .

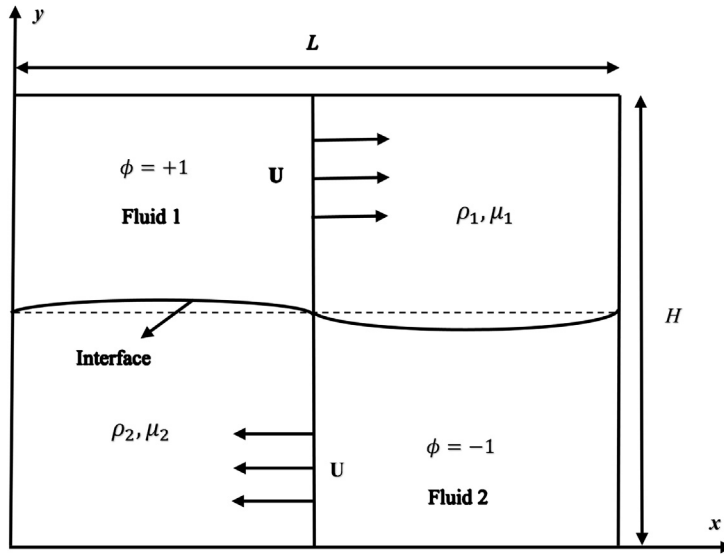


Fig. 2. Schematic diagram of a two fluid system with evolving interface.

As

$$\begin{aligned}
 \nabla \cdot (\nabla \mathbf{U} + (\nabla \mathbf{U})^T) &= \Delta \mathbf{U} + \nabla \cdot (\nabla \mathbf{U})^T \\
 &= \Delta \mathbf{U} + \nabla (\nabla \cdot \mathbf{U}) \\
 &= \Delta \mathbf{U}. \tag{2.7} \\
 \mathbf{U} \cdot \nabla \mathbf{U} &= \nabla \cdot (\mathbf{U}\mathbf{U}) \\
 \mathbf{U} \cdot \nabla \phi &= \nabla \cdot (\mathbf{U}\phi)
 \end{aligned}$$

Now using the identities (2.6), (2.7) in the system (2.5) and taking  $\rho = 1$  we obtain the governing model of two-phase flow of immiscible incompressible fluids in conservative form which is given by

$$\nabla \cdot \mathbf{U} = 0, \tag{2.8a}$$

$$\mathbf{U}_t + \nabla \cdot (\mathbf{U}\mathbf{U}) - \nu \Delta \mathbf{U} + \nabla P = -\lambda \Delta \phi \nabla \phi, \tag{2.8b}$$

$$\phi_t + \nabla \cdot (\mathbf{U}\phi) - \gamma \Delta \phi = \gamma (-\mathcal{F}'(\phi) + \mathcal{L}_m(t)), \tag{2.8c}$$

$$\frac{d}{dt} \int_{\Omega} \phi dx = 0, \tag{2.8d}$$

with the following initial conditions

$$\mathbf{U}|_{t=0} = \mathbf{U}_0, \quad \phi|_{t=0} = \phi_0,$$

and suitable boundary conditions. The Lagrange multiplier  $\mathcal{L}_m(t)$  is responsible for the accumulation of the mass loss. We have used the following formula for the calculation of Lagrange multiplier

$$\mathcal{L}_m(t) = \frac{\int_{\Omega} \mathcal{F}'(\phi) dx}{\int_{\Omega} (1 - \phi^2) dx}. \tag{2.9}$$

### 3. Problem description

When two horizontally parallel fluids of different densities or velocities come into contact, the two-phase KH instability can develop. We consider the flow of two immiscible and incompressible fluids that are constrained by two horizontal boundaries of height  $H$  ( $0 < y < H$ ) as illustrated in Fig. 2. The velocity distribution is taken in such a way that it is opposite on both sides of the interface. The domain is composed of two regions filled with Fluid 1 and Fluid 2 separated by a moving interface. The fluid-fluid interface is subjected to initial sinusoidal perturbations.

### 4. Artificial compressibility method

This section is devoted to the analysis of the artificial compressibility method. Satisfying the incompressibility constraint poses the greatest challenge in solving the incompressible Navier–Stokes equation. In this method, the continuity

equation is modified by adding the pseudo-time derivative of pressure. The dual time-stepping approach is then used to march both in pseudo and physical times together. In this method, we add the artificial compressibility terms to each equation in system (2.8) such as

$$P_\tau + \beta (\nabla \cdot \mathbf{U}) = 0, \tag{4.1a}$$

$$U_\tau + \mathbf{U}_t + \nabla \cdot (\mathbf{U}\mathbf{U}) - \nu \Delta \mathbf{U} + \nabla P = -\lambda \Delta \phi \nabla \phi, \tag{4.1b}$$

$$\phi_\tau + \phi_t + \nabla \cdot (\mathbf{U}\phi) - \gamma \Delta \phi = \gamma (-\mathcal{F}'(\phi) + \mathcal{L}_m(t)). \tag{4.1c}$$

In component form the system (4.1) can be expressed as

$$P_\tau + \beta (u_x + v_y) = 0, \tag{4.2a}$$

$$u_\tau + u_t + (u^2 + P)_x + (uv)_y - \nu (u_{xx} + u_{yy}) = -\lambda \phi_x (\phi_{xx} + \phi_{yy}), \tag{4.2b}$$

$$v_\tau + v_t + (uv)_x + (v^2 + P)_y - \nu (v_{xx} + v_{yy}) = -\lambda \phi_y (\phi_{xx} + \phi_{yy}), \tag{4.2c}$$

$$\phi_\tau + \phi_t + (u\phi)_x + (v\phi)_y - \gamma (\phi_{xx} + \phi_{yy}) = \gamma (-\mathcal{F}'(\phi) + \mathcal{L}_m(t)). \tag{4.2d}$$

In matrix form the system (4.2) can be written as

$$\mathcal{Q}_\tau + \mathcal{I}_m \mathcal{Q}_t + (\mathcal{C} - \mathcal{C}_v)_x + (\mathcal{V} - \mathcal{V}_v)_y = \mathcal{R}, \tag{4.3}$$

with

$$\mathcal{Q} = \begin{bmatrix} P \\ u \\ v \\ \phi \end{bmatrix}, \mathcal{C} = \begin{bmatrix} \beta u \\ u^2 + P \\ uv \\ u\phi \end{bmatrix}, \mathcal{V} = \begin{bmatrix} \beta v \\ uv \\ v^2 + P \\ v\phi \end{bmatrix}, \mathcal{I}_m = \begin{bmatrix} 0 & 0 & 0 & 0 \\ 0 & 1 & 0 & 0 \\ 0 & 0 & 1 & 0 \\ 0 & 0 & 0 & 1 \end{bmatrix},$$

and

$$\mathcal{C}_v = \begin{bmatrix} 0 \\ \nu u_x \\ \nu v_x \\ \gamma \phi_x \end{bmatrix}, \mathcal{V}_v = \begin{bmatrix} 0 \\ \nu u_y \\ \nu v_y \\ \gamma \phi_y \end{bmatrix}, \mathcal{R} = \begin{bmatrix} 0 \\ -\lambda \phi_x (\phi_{xx} + \phi_{yy}) \\ -\lambda \phi_y (\phi_{xx} + \phi_{yy}) \\ \gamma (-\mathcal{F}'(\phi) + \mathcal{L}_m(t)) \end{bmatrix}.$$

In Eq. (4.3),  $\mathcal{Q}$  stands for the solution vector,  $u$  and  $v$  are Cartesian velocity components,  $P$  is the modified pressure,  $\phi$  is the phase variable,  $\nu$  is the viscosity constant,  $\beta$  is the artificial compressibility constant,  $\tau$  is the pseudo-time, and  $t$  is the physical time. Matrix  $\mathcal{I}_m$  is a special case of the identity matrix. The nonlinear component in the phase field equation and the capillary effect, contribute  $\mathcal{R}$ .

The equations have taken on a hyperbolic type result of the inclusion of artificial compressibility terms. Using hyperbolic theory, we can find the eigenvalues and eigenvectors of the convective fluxes. To do this, we start by determining the Jacobian matrices  $\mathcal{A}$  and  $\mathcal{B}$  from the flux vectors given by

$$\mathcal{A} = \frac{\partial \mathcal{C}}{\partial \mathcal{Q}} = \begin{bmatrix} 0 & \beta & 0 & 0 \\ 1 & 2u & 0 & 0 \\ 0 & v & u & 0 \\ 0 & \phi & 0 & u \end{bmatrix}, \mathcal{B} = \frac{\partial \mathcal{V}}{\partial \mathcal{Q}} = \begin{bmatrix} 0 & 0 & \beta & 0 \\ 0 & v & u & 0 \\ 1 & 0 & 2v & 0 \\ 0 & 0 & \phi & v \end{bmatrix}.$$

Similar to this, the Jacobian matrices  $\mathcal{A}_v$  and  $\mathcal{B}_v$  of the viscous flux vectors  $\mathcal{C}_v$  and  $\mathcal{V}_v$  are provided by

$$\mathcal{A}_v = \frac{\partial \mathcal{C}_v}{\partial \mathcal{Q}} = \text{diag}(0, \nu, \nu, \gamma) \partial_x, \text{ and } \mathcal{B}_v = \frac{\partial \mathcal{V}_v}{\partial \mathcal{Q}} = \text{diag}(0, \nu, \nu, \gamma) \partial_y. \tag{4.4}$$

### 5. Numerical discretization

This section is devoted to the discretization of the governing equations.

#### 5.1. Spatial discretization

In this section, Eq. (4.3) is discretized in spatial coordinates. A high-order finite difference scheme for hyperbolic conservation laws is used for the discretization of the inviscid flux derivatives. The uniform meshes are employed in each direction. As the model is nonlinear and stiff, therefore an effective discretization of the convective and source terms is a major challenge. Therefore, we used a variant [29] of the weighted essentially non-oscillatory (WENO) scheme [26] for the discretization of the convective terms to circumvent the difficulty posed by the stiffness of the interface. The conventional 2nd-order central finite difference schemes are used to discretize the diffusion and surface tension terms (see Ref. [28] for details).

Let the mesh size in the  $x$ -direction is  $h$  and denote  $x_j = jh$ . We will approximate the convective flux  $C$  at  $x_j$  using the WENO fifth-order scheme as

$$C_x = \frac{\hat{C}_{j+\frac{1}{2}} - \hat{C}_{j-\frac{1}{2}}}{h} \tag{5.1}$$

where  $\hat{C}_{j+\frac{1}{2}}$  and  $\hat{C}_{j-\frac{1}{2}}$  are the numerical fluxes. The Lax-Friedrichs split fluxes in the  $s$ th characteristic field are given by:

$$f_k^{s\pm} = \frac{f_k^s \pm \alpha_s W_k^s}{2}, \quad k = j - 2, \dots, j + 3, \tag{5.2}$$

with

$$f_k^s = \mathbf{L}_{j+\frac{1}{2}}^s \cdot C_k, \quad W_k^s = \mathbf{L}_{j+\frac{1}{2}}^s \cdot Q_k,$$

where  $\mathbf{L}_{j+\frac{1}{2}}^s$  is the  $s$ th left eigenvector, and  $\alpha_s$  is the maximum magnitude of the  $s$ th eigenvalue of Jacobian matrix  $\mathcal{A}_{k+\frac{1}{2}}$  over the range of  $(k = j - 2, \dots, j + 2)$  for the local flux splitting. The positive part of the WENO numerical flux  $\hat{f}_{j+\frac{1}{2}}^{s+}$  is

$$\begin{aligned} \hat{f}_{j+\frac{1}{2}}^{s+} = & \omega_0^+ \left( \frac{2}{6} f_{j-2}^{s+} - \frac{7}{6} f_{j-1}^{s+} + \frac{11}{6} f_j^{s+} \right) + \omega_1^+ \left( -\frac{1}{6} f_{j-1}^{s+} + \frac{5}{6} f_j^{s+} + \frac{2}{6} f_{j+1}^{s+} \right) \\ & + \omega_2^+ \left( \frac{2}{6} f_j^{s+} + \frac{5}{6} f_{j+1}^{s+} - \frac{1}{6} f_{j+2}^{s+} \right), \end{aligned} \tag{5.3}$$

where

$$\omega_k^+ = \frac{\alpha_k^+}{\alpha_0^+ + \alpha_1^+ + \alpha_2^+}, \quad k = 0, 1, 2$$

$$\alpha_0^+ = \frac{1}{10} (\varepsilon + S_0^+)^{-2}, \quad \alpha_1^+ = \frac{6}{10} (\varepsilon + S_1^+)^{-2}, \quad \alpha_2^+ = \frac{3}{10} (\varepsilon + S_2^+)^{-2}, \quad \varepsilon = 10^{-6}$$

and

$$\begin{aligned} S_0^+ &= \frac{13}{12} (f_{j-2}^{s+} - 2f_{j-1}^{s+} + f_j^{s+})^2 + \frac{1}{4} (f_{j-2}^{s+} - 4f_{j-1}^{s+} + 3f_j^{s+})^2 \\ S_1^+ &= \frac{13}{12} (f_{j-1}^{s+} - 2f_j^{s+} + f_{j+1}^{s+})^2 + \frac{1}{4} (f_{j-1}^{s+} - f_{j+1}^{s+})^2 \\ S_2^+ &= \frac{13}{12} (f_j^{s+} - 2f_{j+1}^{s+} + f_{j+2}^{s+})^2 + \frac{1}{4} (3f_j^{s+} - 4f_{j+1}^{s+} + f_{j+2}^{s+})^2. \end{aligned}$$

In a similar manner the numerical flux  $\hat{f}_{j+\frac{1}{2}}^{s-}$  for the negative part is

$$\begin{aligned} \hat{f}_{j+\frac{1}{2}}^{s-} = & \omega_0^- \left( -\frac{1}{6} f_{j-1}^{s-} + \frac{5}{6} f_j^{s-} + \frac{2}{6} f_{j+1}^{s-} \right) + \omega_1^- \left( \frac{2}{6} f_j^{s-} + \frac{5}{6} f_{j+1}^{s-} - \frac{1}{6} f_{j+2}^{s-} \right) \\ & + \omega_2^- \left( \frac{11}{6} f_{j+1}^{s-} - \frac{7}{6} f_{j+2}^{s-} + \frac{2}{6} f_{j+3}^{s-} \right), \end{aligned} \tag{5.4}$$

where

$$\omega_k^- = \frac{\alpha_k^-}{\alpha_0^- + \alpha_1^- + \alpha_2^-}, \quad k = 0, 1, 2$$

$$\alpha_0^- = \frac{3}{10} (\varepsilon + S_0^-)^{-2}, \quad \alpha_1^- = \frac{6}{10} (\varepsilon + S_1^-)^{-2}, \quad \alpha_2^- = \frac{1}{10} (\varepsilon + S_2^-)^{-2}, \quad \varepsilon = 10^{-6}$$

and

$$\begin{aligned} S_0^- &= \frac{13}{12} (f_{j-1}^{s-} - 2f_j^{s-} + f_{j+1}^{s-})^2 + \frac{1}{4} (f_{j-1}^{s-} - 4f_j^{s-} + 3f_{j+1}^{s-})^2 \\ S_1^- &= \frac{13}{12} (f_j^{s-} - 2f_{j+1}^{s-} + f_{j+2}^{s-})^2 + \frac{1}{4} (f_j^{s-} - f_{j+2}^{s-})^2 \\ S_2^- &= \frac{13}{12} (f_{j+1}^{s-} - 2f_{j+2}^{s-} + f_{j+3}^{s-})^2 + \frac{1}{4} (3f_{j+1}^{s-} - 4f_{j+2}^{s-} + f_{j+3}^{s-})^2. \end{aligned}$$

The obtained numerical fluxes are transformed back to the physical space by

$$\hat{c}_{j+\frac{1}{2}} = \sum_{s=1}^4 \hat{f}_{j+\frac{1}{2}}^s \mathbf{R}_{j+\frac{1}{2}}^s = \sum_{s=1}^4 \left( \hat{f}_{j+\frac{1}{2}}^{s+} + \hat{f}_{j+\frac{1}{2}}^{s-} \right) \mathbf{R}_{j+\frac{1}{2}}^s. \tag{5.5}$$

where  $\mathbf{R}_{j+\frac{1}{2}}^s$  represent the  $s$ th right eigenvector of the Jacobian matrix  $\mathcal{A}_{j+\frac{1}{2}}$ .

### 5.2. Time discretization

Consider Eq. (4.3) that contains pseudo-time and the physical time derivative term, therefore both terms will be discretized using different formulas. Using 1st-order forward difference formula for the pseudo-time derivative term and second-order three points formula for the physical time derivative term in Eq. (4.3), we have

$$\frac{\Delta \mathcal{Q}^{n+1,m}}{\Delta \tau} + \mathcal{I}_m \frac{-3\mathcal{Q}^{n+1,m+1} + 4\mathcal{Q}^n - \mathcal{Q}^{n-1}}{2\Delta t} + [(C - c_v)_x + (\mathcal{V} - \mathcal{V}_v)_y]^{n+1,m+1} = \mathcal{R}^{n+1,m}. \tag{5.6}$$

The superscripts  $n, m$  signify the level of physical time and pseudo-time respectively in Eq. (5.6), where  $\Delta \mathcal{Q}^{n+1,m} = \mathcal{Q}^{n+1,m+1} - \mathcal{Q}^{n+1,m}$ . Here,  $\Delta \tau$  and  $\Delta t$  represent the pseudo and physical time steps, respectively and  $\mathcal{R}$  is the residual terms containing the surface tension terms and phase field source terms as in Eq. (4.3). The pseudo-time is used to marched until the divergence free velocity is attained. The nonlinear terms  $\mathcal{C}, \mathcal{V}$  at the pseudo-time  $m + 1$  are linearized using Taylor series expansion as given below

$$\begin{aligned} c^{m+1} &\approx c(\mathcal{Q}^m) + \left( \frac{\partial c}{\partial \mathcal{Q}} \right)^m (\mathcal{Q}^{m+1} - \mathcal{Q}^m) \\ &= c^m + \mathcal{A}^m \Delta \mathcal{Q}^m. \end{aligned} \tag{5.7}$$

and

$$\begin{aligned} \mathcal{V}^{m+1} &\approx \mathcal{V}(\mathcal{Q}^m) + \left( \frac{\partial \mathcal{V}}{\partial \mathcal{Q}} \right)^m (\mathcal{Q}^{m+1} - \mathcal{Q}^m) \\ &= \mathcal{V}^m + \mathcal{B}^m \Delta \mathcal{Q}^m. \end{aligned} \tag{5.8}$$

Using Eqs. (5.7) and (5.8) in Eq. (5.6) and omitting the superscript  $n + 1$ , we have the following linear system of equations

$$\begin{aligned} &\left[ \mathcal{I} + 1.5 \frac{\Delta \tau}{\Delta t} \mathcal{I}_m + \Delta \tau ((\mathcal{A} - \mathcal{A}_v)_x + (\mathcal{B} - \mathcal{B}_v)_y) \right]^m \Delta \mathcal{Q}^m \\ &= -\Delta \tau ((C - c_v)_x + (\mathcal{V} - \mathcal{V}_v)_y - \mathcal{R})^m - \frac{\Delta \tau}{\Delta t} \mathcal{I}_m (1.5\mathcal{Q}^m - 2\mathcal{Q}^n + 0.5\mathcal{Q}^{n-1}) \\ &= \mathbf{R}^m. \end{aligned} \tag{5.9}$$

It is possible to diagonalize  $\mathcal{A} = \mathcal{X} \Lambda_{\mathcal{A}} \mathcal{X}^{-1}$ , and  $\mathcal{B} = \mathcal{Y} \Lambda_{\mathcal{B}} \mathcal{Y}^{-1}$  due to the hyperbolic nature of Eq. (4.3), where  $\mathcal{X}$  and  $\mathcal{Y}$  are matrices of the corresponding eigenvectors respectively. Further, the matrices  $\mathcal{A}$ , and  $\mathcal{B}$  can be partitioned into positive and negative parts based on the sign of the eigenvalues, when first-order upwind scheme is used.

$$\left[ \mathcal{I} + 1.5 \frac{\Delta \tau}{\Delta t} \mathcal{I}_m + \Delta \tau (\delta_x^- \mathcal{A}^+ + \delta_x^+ \mathcal{A}^- - \delta_x \mathcal{A}_v) + \Delta \tau (\delta_y^- \mathcal{B}^+ + \delta_y^+ \mathcal{B}^- - \delta_y \mathcal{B}_v) \right]^m \Delta \mathcal{Q}^m = \mathbf{R}^m. \tag{5.10}$$

Denoting  $\mathcal{H} = (1 + 1.5 \frac{\Delta \tau}{\Delta t}) \mathcal{I}$ ,  $\mu_m = \max(\mu, \gamma)$  and making use of the denationalization which save time we replace  $\mathcal{I}_m$  by  $\mathcal{I}$  and  $\text{diag}(0, \mu, \mu, \gamma)$  by  $\max(\mu, \gamma) \mathcal{I}$  in the LHS of Eq. (5.10), we obtain the following equation

$$[\mathcal{H} + \Delta \tau (\delta_x^- \mathcal{X} \Lambda_{\mathcal{A}}^+ \mathcal{X}^{-1} + \delta_x^+ \mathcal{X} \Lambda_{\mathcal{A}}^- \mathcal{X}^{-1} - \mu_m \mathcal{I} \delta_x^2) + \Delta \tau (\delta_y^- \mathcal{Y} \Lambda_{\mathcal{B}}^+ \mathcal{Y}^{-1} + \delta_y^+ \mathcal{Y} \Lambda_{\mathcal{B}}^- \mathcal{Y}^{-1} - \mu_m \mathcal{I} \delta_y^2)]^m \Delta \mathcal{Q}^m = \mathbf{R}^m. \tag{5.11}$$

Now adding the cross derivative term to the LHS, we have the following approximate factorization form

$$\begin{aligned} &[\mathcal{H} + \Delta \tau (\delta_x^- \mathcal{X} \Lambda_{\mathcal{A}}^+ \mathcal{X}^{-1} + \delta_x^+ \mathcal{X} \Lambda_{\mathcal{A}}^- \mathcal{X}^{-1} - \mu_m \mathcal{I} \delta_x^2)] \mathcal{H}^{-1} \times \\ &[\mathcal{H} + \Delta \tau (\delta_y^- \mathcal{Y} \Lambda_{\mathcal{B}}^+ \mathcal{Y}^{-1} + \delta_y^+ \mathcal{Y} \Lambda_{\mathcal{B}}^- \mathcal{Y}^{-1} - \mu_m \mathcal{I} \delta_y^2)] \Delta \mathcal{Q}^m \\ &= \mathbf{R}^m. \end{aligned} \tag{5.12}$$

The linear system (5.12) is solved for  $\Delta \mathcal{Q}^m = \mathcal{Q}^{m+1} - \mathcal{Q}^m$  using the Alternating Direction Implicit (ADI) technique in each direction, yielding a solution to a tri-diagonal system of the form

$$a_j \Delta \mathcal{U}_{j-1} + b_j \Delta \mathcal{U}_j + c_j \Delta \mathcal{U}_{j+1} = r_j, \quad j = 1, \dots, jmax - 1.$$

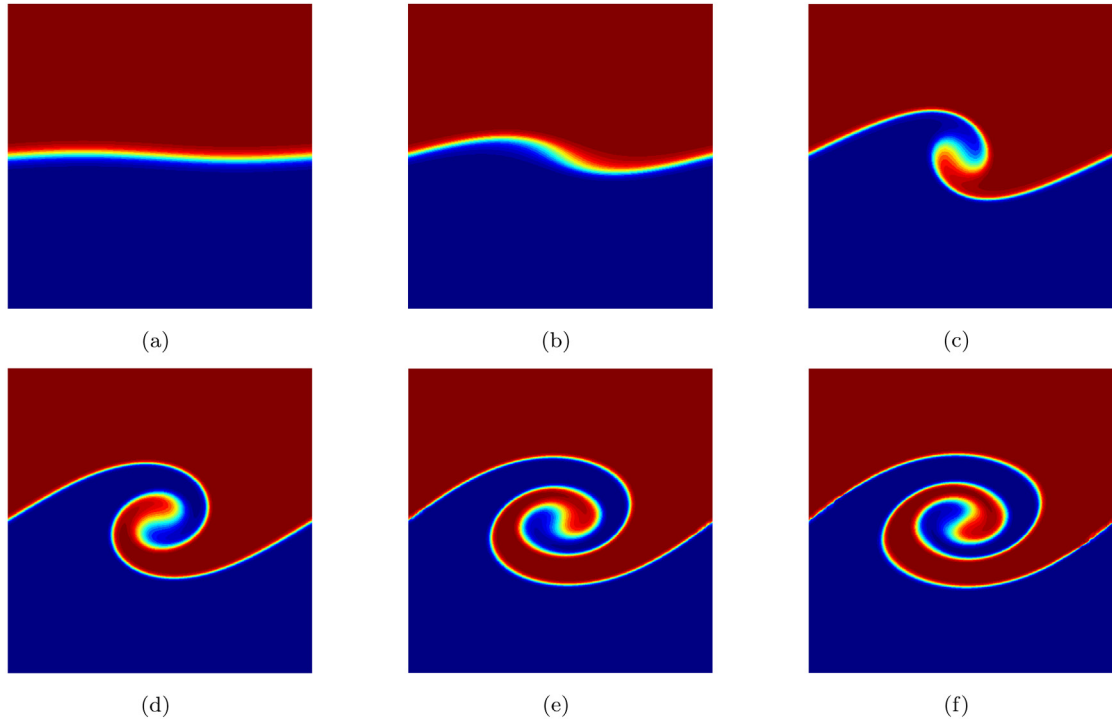


**Fig. 3.** Temporal evolution of the phase-field perturbed sinusoidally at (a)  $t = 0$  (b)  $t = 0.5$  (c)  $t = 0.8$  (d)  $t = 1$  (e)  $t = 1.2$  (f)  $t = 1.3$  for case (i) when  $\nu = 0.0001$  and  $\gamma = 0.0001$ .

### 6. Results and discussions

In this section, multiple numerical experiments are presented to demonstrate the dynamics of the two-phase KH instability. For each example, parameter values are provided. For each problem, we provide both the velocity-field and phase-field variable in the domain  $\Omega = [0, 1] \times [0, 1]$ . The compressibility parameter  $\beta = 200$  and the thickness of the interface  $\epsilon = 0.02$  are used to enable pseudo-time marching, respectively, at a maximum number of sub-iterations of 100. The mesh size is chosen comparable to the thickness of the interface to capture the interface's dynamics effectively. Four examples are simulated for the validation of the method given in the subsection below.

#### 6.1. Dynamics of single mode sinusoidal perturbation

This example shows the dynamics of a sinusoidal perturbation between two fluids with a single mode. The grid points on the  $x$ - and  $y$ -axes are 513 each. The time step is set to 0.001, and the other parameters are fixed as follows:

**Case (i)**

$$\lambda = 0.0001, \quad \nu = 0.0001, \quad 0.001 \text{ and } \gamma = 0.0001, \quad 0.001.$$

The initial velocity-field and phase-field variable are given by

$$u^0(x, y) = \tanh \left[ \frac{(y - 0.5 - 0.01 \sin(2\pi x))}{\sqrt{2}\epsilon} \right], \quad v^0(x, y) = 0, \quad \phi^0(x, y) = u^0(x, y).$$

**Case (ii)**

$$\lambda = 0.0001, \quad \nu = 0.001, \text{ and } \gamma = 0.001.$$

The initial velocity-field and phase-field variable are given by

$$u^0(x, y) = 0, \quad v^0(x, y) = 0, \quad \phi^0(x, y) = \tanh \left[ \frac{(y - 0.5 - 0.01 \sin(2\pi x))}{\sqrt{2}\epsilon} \right].$$

Fig. 3 shows the dynamics of the interface's temporal evolution at different times. The initial perturbation grows gradually and there is a rolling up of the interface at the center of the domain. This rolling up of the interface gets a spiral shape at a later time as shown in Fig. 3. The vorticity evolution is given in Fig. 4. The top and bottom fluid flow in opposite

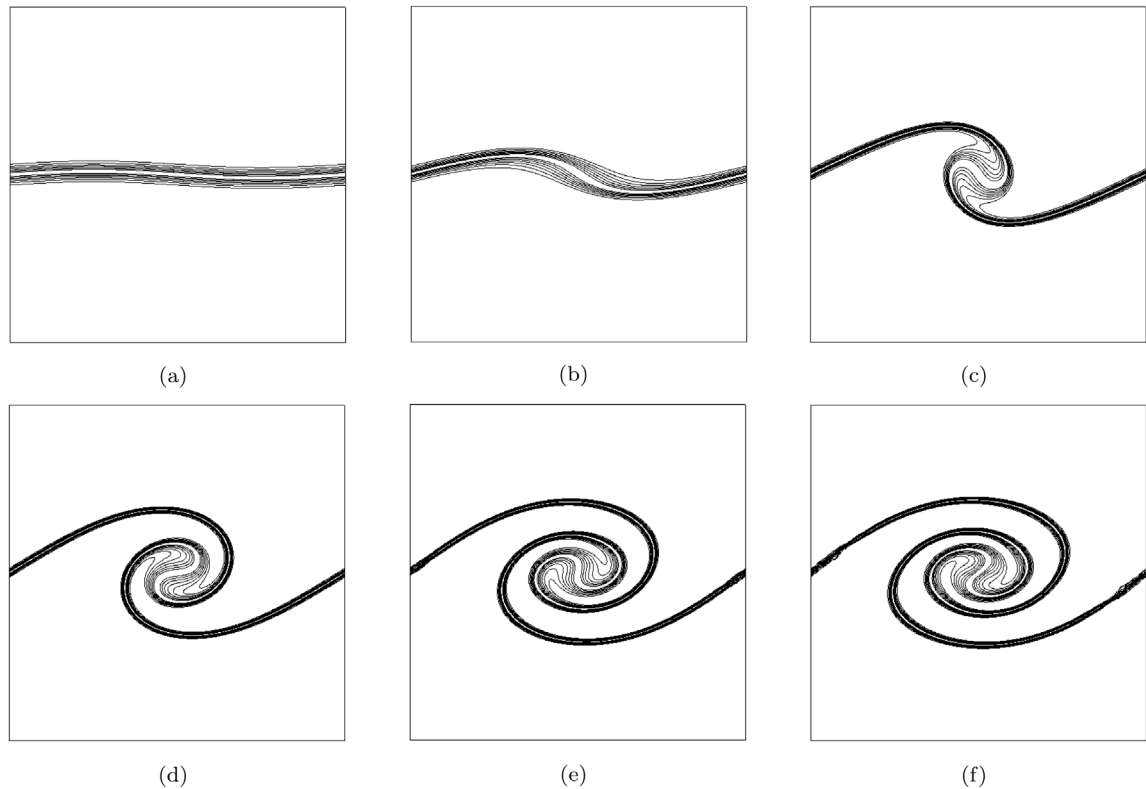


**Fig. 4.** Single mode vorticity dynamics at time (a)  $t = 0$  (b)  $t = 0.5$  (c)  $t = 0.8$  (d)  $t = 1$  (e)  $t = 1.2$  (f)  $t = 1.3$  for case (i) when  $\nu = 0.0001$  and  $\gamma = 0.0001$ .

directions and the vorticity moves to the center of the domain. Fig. 5 depicts the dynamics of the flow field with the evolving interface. The dynamics of the interface and vorticity profile is qualitatively comparable with the results given in Ref. [8]. It is observed from Fig. 6 that rolling of the interface is slow when the viscosity is increased. Fig. 7 shows the vector plot of dynamic of the interface for case (ii) when the velocity is zero. A slight variation in the velocity is observed near the interface. We need to do several experiments to determine a rule of thumb for selecting the artificial compressibility factor  $\beta$ , which determines the convergence rate and stability of the artificial compressibility approach. As such, the literature provided a variety of methods for determining the optimal  $\beta$ . See, for instance, the works cited in Refs. [30–34]. In particular, Ref. [34] provided a precise lower bound of  $\beta$  to prevent viscous effects from coupling the pseudo-pressure waves, and a reasonable upper bound for the approximation factorization errors not to screw up the accuracy of the computations. In most cases, however, it is not possible to predict in advance which option will out to be the best. Convergence rates vary when  $\beta$  is varied; optimal rates are achieved at  $\beta = 150$  and  $200$ . The convergence for several values of  $\beta$  is shown in Fig. 8. If the optimal CFL number is selected for each value of  $\beta$  in the range of 50–250, it is clear that these choices do not significantly alter the convergence rate. Hence, we can save a lot of time fine-tuning  $\beta$ . In most cases, a  $\beta$  value of 200 is acceptable.

### 6.2. Grid convergence study

For numerical convergence of the scheme with respect to grid size, we computed with different grid points. We take one sample initial condition of a single mode sinusoidal perturbation and perform the simulation using  $65 \times 65$ ,  $129 \times 129$ ,  $257 \times 257$ , and  $513 \times 513$  grid points. Fig. 9 shows the dynamics of the interface obtained using  $65 \times 65$  (red),  $129 \times 129$  (blue),  $257 \times 257$  (pink), and  $513 \times 513$  (green). It is clear that the results of grid refinement have converged for  $129 \times 129$  and above grids by considering solution at  $513 \times 513$  grids as a true solution (green line) in Fig. 9.

### 6.3. Dynamics of double mode sinusoidal perturbation

In this example, we have taken a double mode sinusoidal perturbation at the interface. The domain and parameter values are same as in the previous problem. The dynamics of the interface and vorticity profiles are given in Figs. 10 and 11 respectively. Instead of one rolling-up of the interface as in previous problem, now two rolled vortices of the interface formed and it takes the spiral shape. Fig. 12 shows the dynamic of the velocity-field around the moving interface.

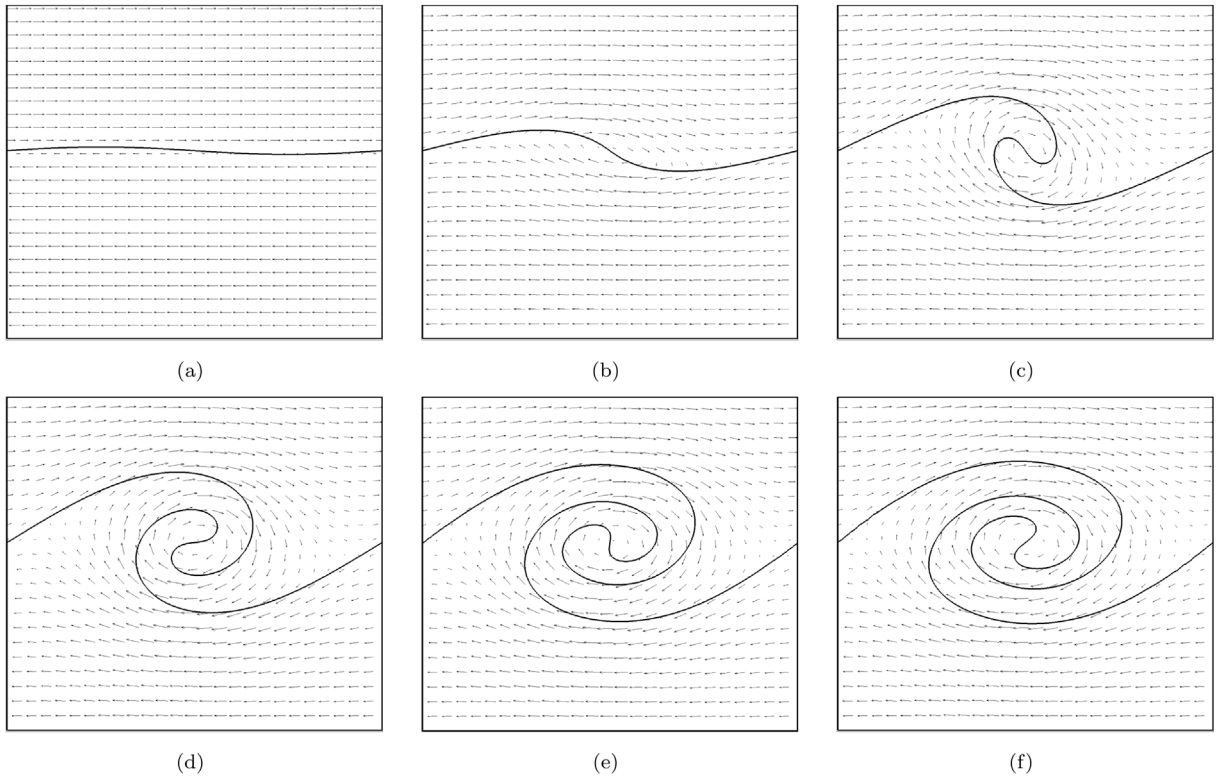


**Fig. 5.** Vector plot of the single mode sinusoidal perturbation at (a)  $t = 0$  (b)  $t = 0.5$  (c)  $t = 0.8$  (d)  $t = 1$  (e)  $t = 1.2$  (f)  $t = 1.3$  for case (i) when  $\nu = 0.0001$  and  $\gamma = 0.0001$ .

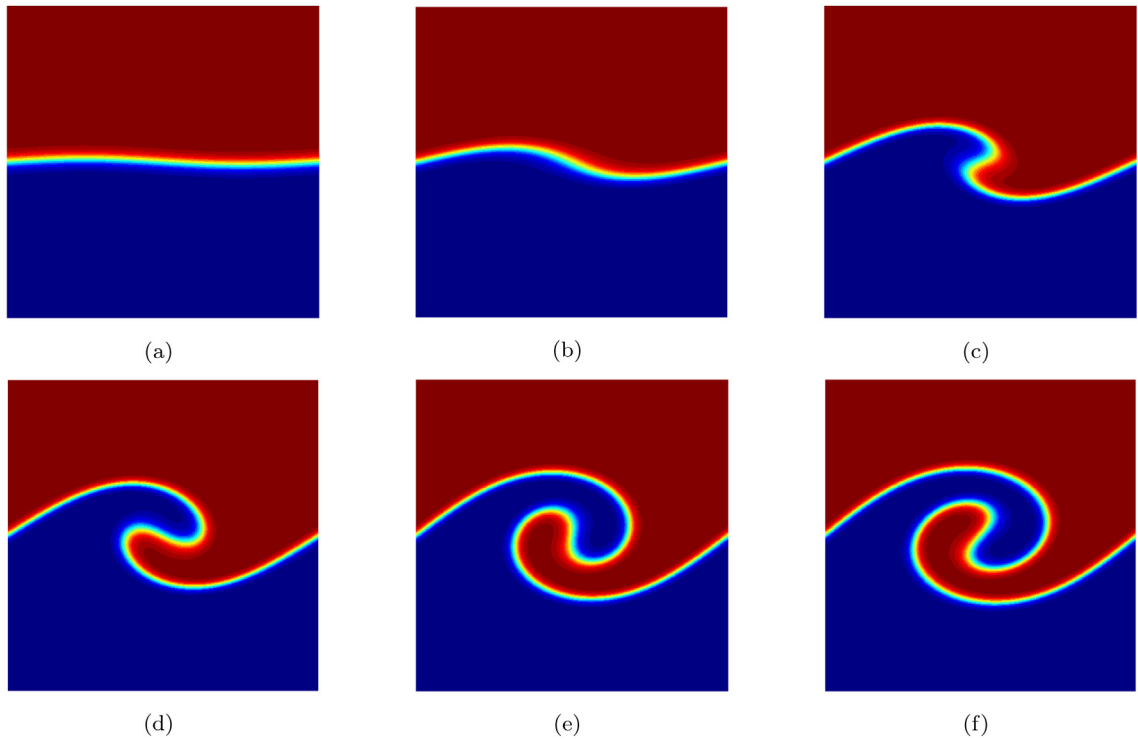


**Fig. 6.** Temporal evolution of the phase-field perturbed sinusoidally at (a)  $t = 0$  (b)  $t = 0.5$  (c)  $t = 0.8$  (d)  $t = 1$  (e)  $t = 1.2$  (f)  $t = 1.3$  for case (i) when  $\nu = 0.001$  and  $\gamma = 0.001$ .

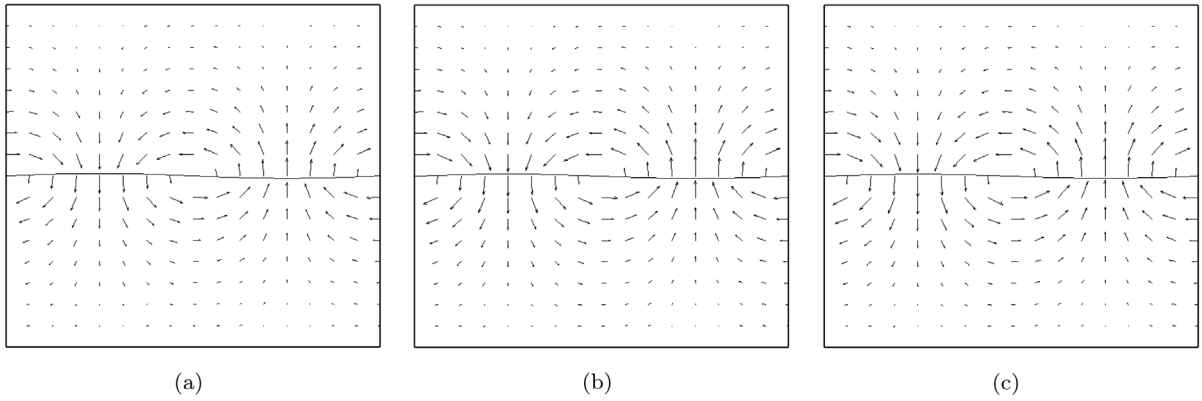


Fig. 7. Vector plot of the single mode sinusoidal perturbation at (a)  $t = 1.0$  (b)  $t = 1.2$  (c)  $t = 1.3$  for case (ii).

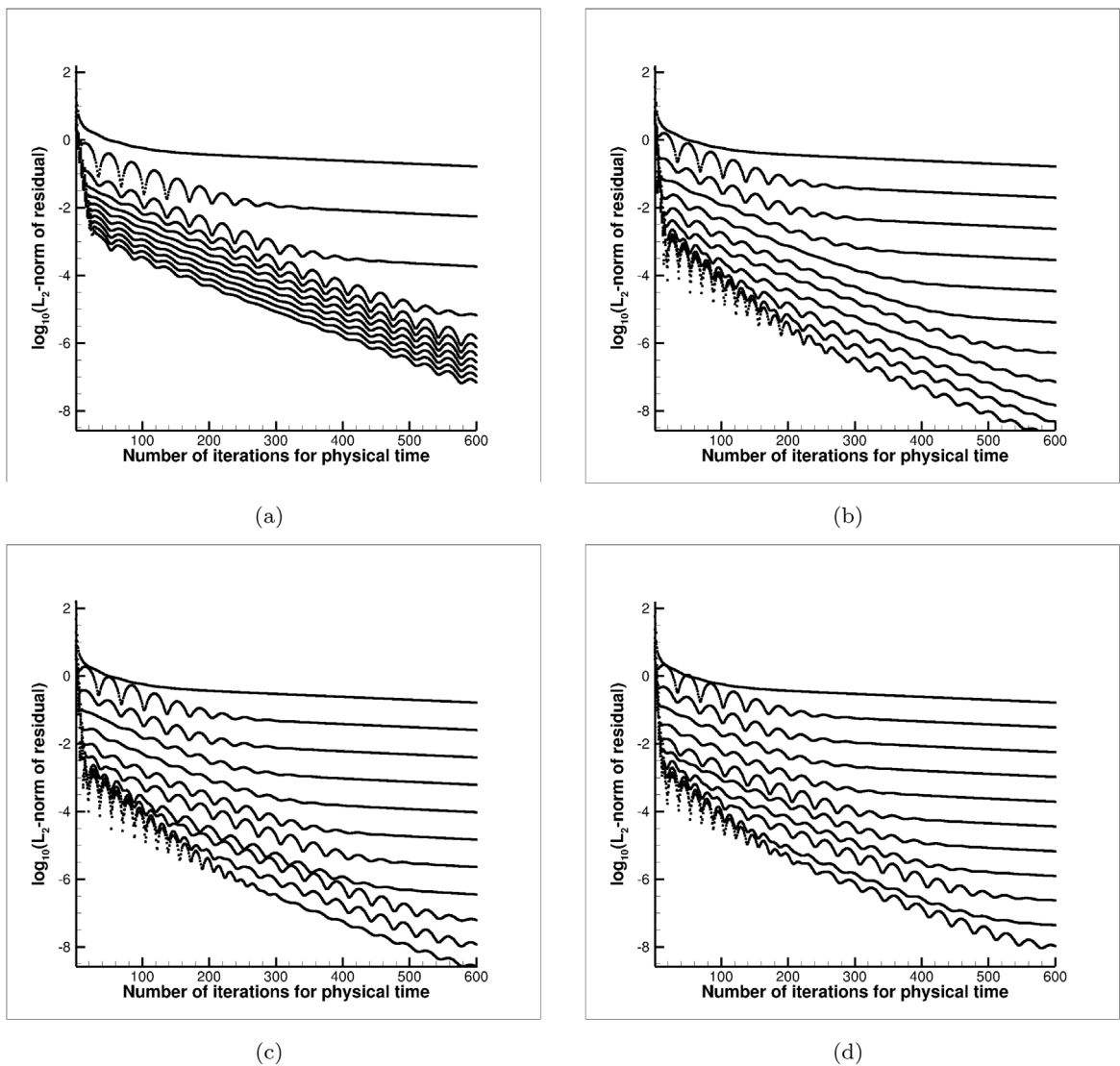
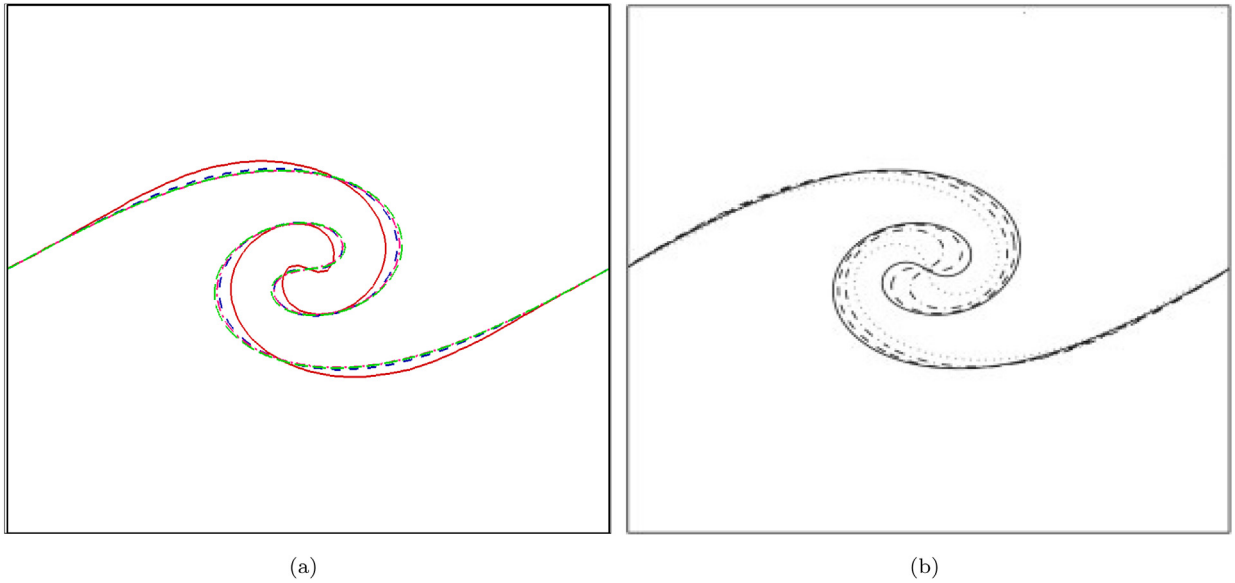
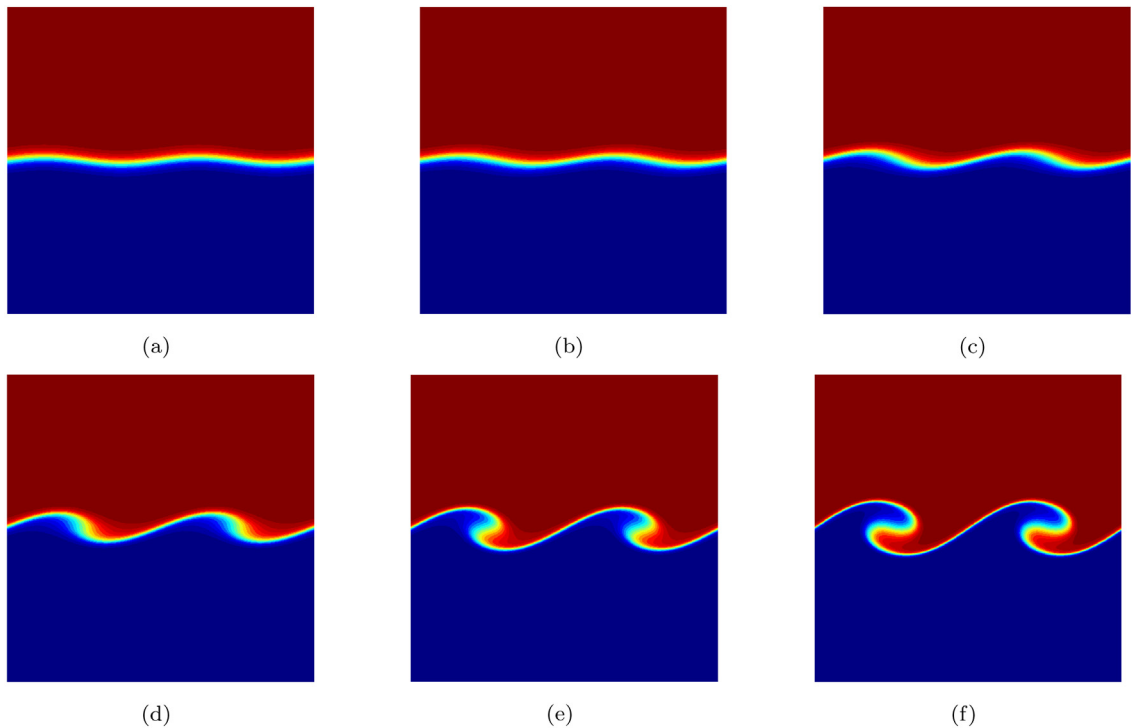


Fig. 8. Residual plot of the single mode sinusoidal perturbation at (a)  $\beta = 50$  (b)  $\beta = 150$  (c)  $\beta = 200$  (d)  $\beta = 250$ .



**Fig. 9.** Dynamic of the interface using  $65 \times 65$  (red),  $129 \times 129$  (blue),  $257 \times 257$  (pink), and  $513 \times 513$  (green) at  $t = 1$  (a) present results (b) results in [8]. The agreement is good.



**Fig. 10.** Phase-field dynamics with a double mode sinusoidal interface perturbation at time (a)  $t = 0$  (b)  $t = 0.1$  (c)  $t = 0.2$  (d)  $t = 0.3$  (e)  $t = 0.4$  (f)  $t = 0.5$ .

#### 6.4. Effect of the surface tension

In this subsection, we investigate the surface tension effects on the dynamic of the KH instability. The domain and initial condition for velocity and phase-field variable are same as in the case of double mode sinusoidal perturbation. In first simulation, we take the parameters value as  $N_x = N_y = 513$ ,  $\Delta t = 0.0005$ ,  $\lambda = 0.001$ ,  $\gamma = 0.001$ . In the second part

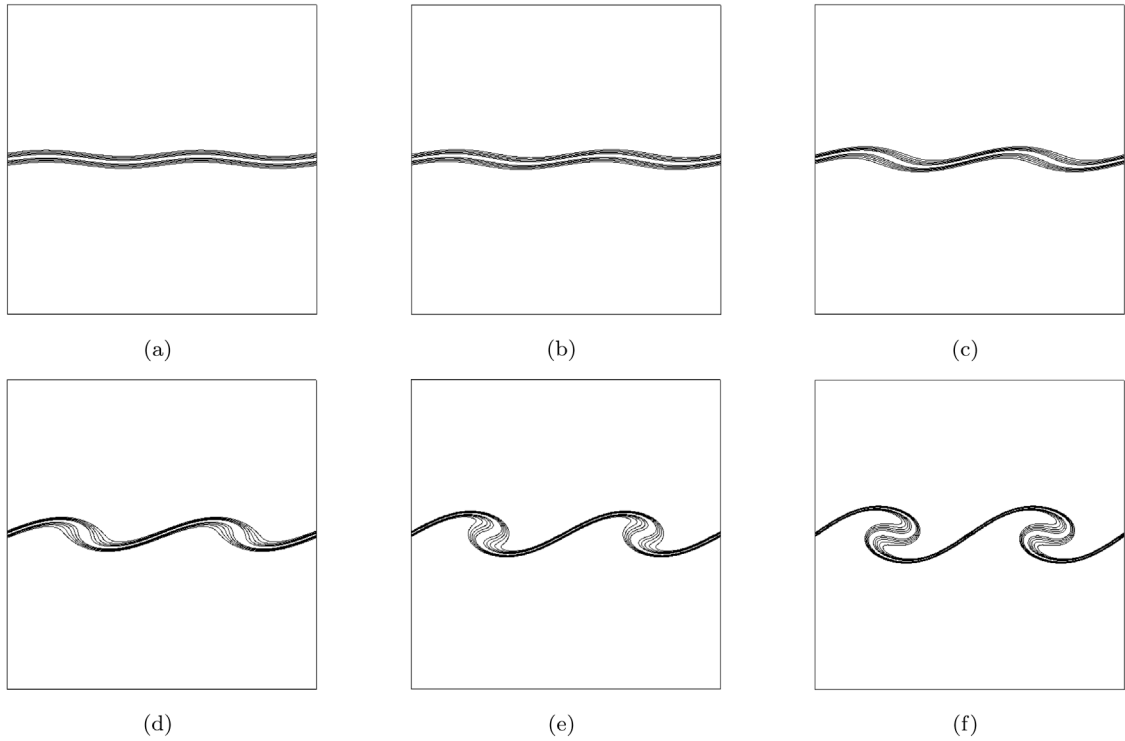


**Fig. 11.** Double mode vorticity contour dynamics at time (a)  $t = 0$  (b)  $t = 0.1$  (c)  $t = 0.2$  (d)  $t = 0.3$  (e)  $t = 0.4$  (f)  $t = 0.5$ .

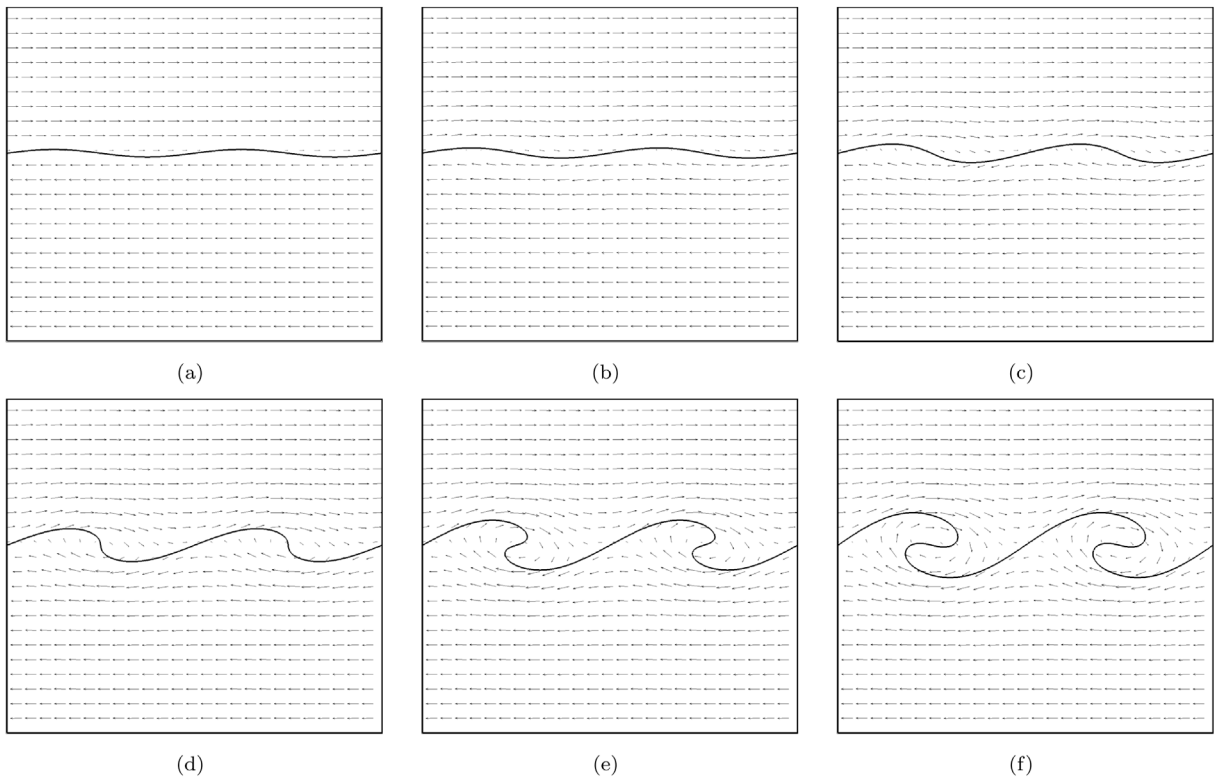


**Fig. 12.** Vector plot simulation of the double mode sinusoidal perturbation at (a)  $t = 0$  (b)  $t = 0.1$  (c)  $t = 0.2$  (d)  $t = 0.3$  (e)  $t = 0.4$  (f)  $t = 0.5$ .

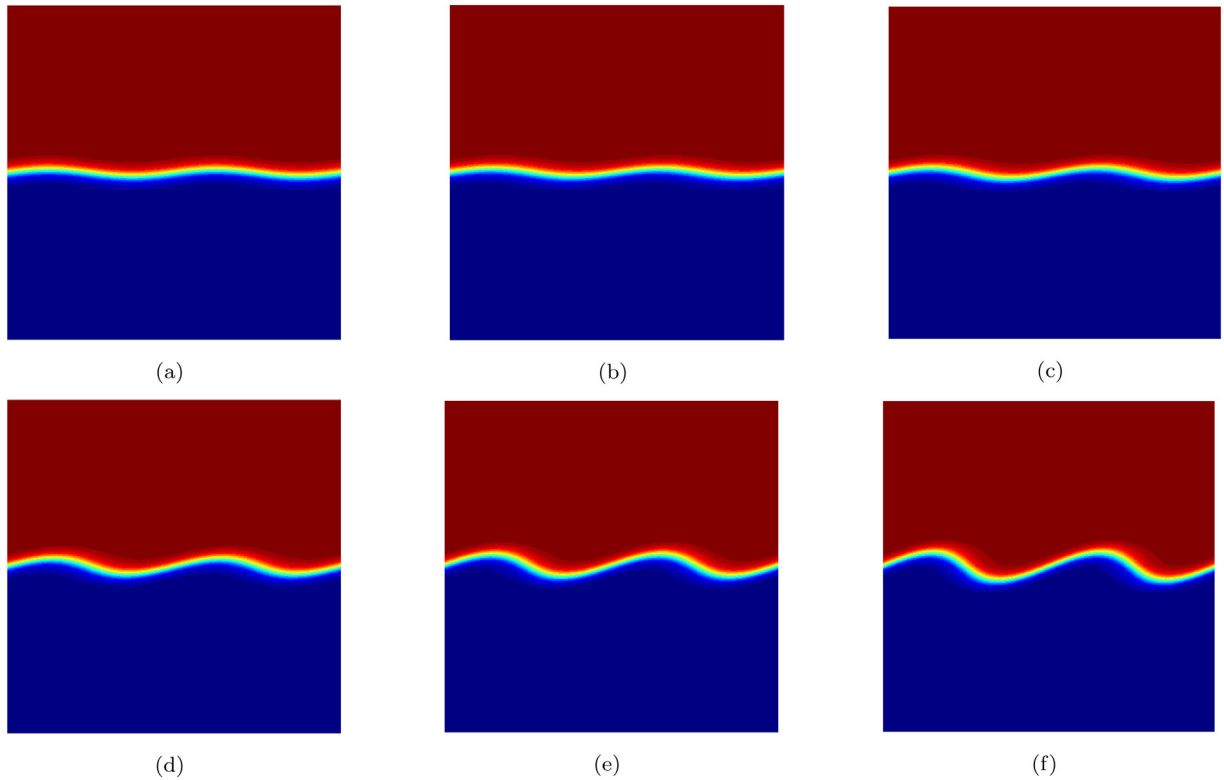


**Fig. 13.** Dynamics of the interface for  $\lambda = 0.001$  at time (a)  $t = 0$  (b)  $t = 0.1$  (c)  $t = 0.2$  (d)  $t = 0.3$  (e)  $t = 0.4$  (f)  $t = 0.5$ .

of simulation, we take the  $N_x = N_y = 257$ ,  $\Delta t = 0.005$ ,  $\lambda = 0.01$ ,  $\gamma = 0.01$ , where  $N_x, N_y$  denotes the number of grid points in  $x$  and  $y$  direction. The simulation results are given in Figs. 13 and 14 for first and second part of the simulations respectively. It is observed that when the surface tension is increased the rolling up of the interface is slow down.

Some of the limitations of the current studies are as follows; First, the convergence is slow when the interfacial width  $\epsilon$  is small which is in fact, common to the diffusive interface method. The interfacial width cannot be arbitrarily small, but it should be comparable to the mesh size to form a regular (not stiff) problem and is also true for other numerical methods like projection method, fully coupled method. Second, the numerical scheme is the traditional approximate factorization scheme like the ADI method. In 2D, it is unconditionally stable only for linear convection equations. However, due to nonlinear effects with the addition of surface tension terms and nonlinear terms occurring in the phase-field equation, the sub-iteration number used is as large as 100 for the residuals to reduce by two orders of magnitude in the initial stage of simulation and 4 orders of magnitudes in most times of the simulation. The 100 iterations are not efficient. We expect it can be reduced to a few sub-iterations if using other algebraic solvers like the GMRES method or the line Gauss–Seidel relaxation method.

## 7. Conclusion

The artificial compressibility approach has been implemented to study the two-phase KH instability problem. The governing system composed of the conserved Allen–Cahn and incompressible Navier–Stokes equations was adopted for studying the KH instability numerically. The implicit solution to the resulting linear system of equations was found using the Beam–Warming approximation factorization scheme. Different simulations for the single/double mode sinusoidal perturbation of the interface were carried out. The grid convergence study and the effect of the surface tension on the dynamics of the interface. The rolling up of the interface was observed to have a spiral-like shape at a later time. It was also noted that by increasing the value of surface tension the rolling of the interface is slowed down.

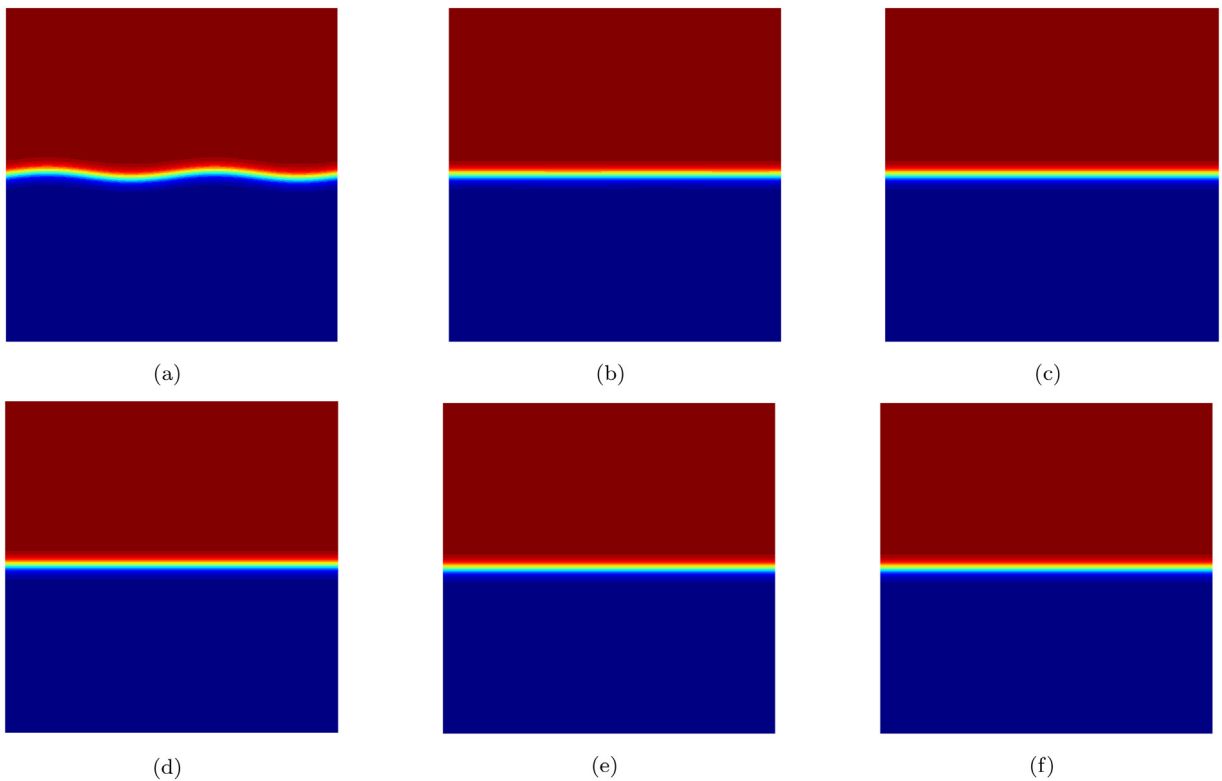


**Fig. 14.** Dynamics of the interface for  $\lambda = 0.01$  at time (a)  $t = 0$  (b)  $t = 1$  (c)  $t = 1.5$  (d)  $t = 2$  (e)  $t = 2.5$  (f)  $t = 3$ .

### CRediT authorship contribution statement

**Abdullah Shah:** Conceptualization, Project administration, Supervision, Writing – review & editing. **Muhammad Sohaib:** Formal analysis, Methodology, Investigation, Validation, Visualization, Writing–original draft. **Li Yuan:** Visualization, Reviewing the draft, Editing, Supervision, Critical analysis.

### Declaration of competing interest

The authors declare that they have no known competing financial interests or personal relationships that could have appeared to influence the work reported in this paper.

### Data availability

Data will be made available on request.

### Acknowledgments

The work of Muhammad Sohaib is financially supported by the Higher Education Commission (HEC) Pakistan under Faculty Development Program (Indigenous). He extends his gratitude to Bacha Khan University Charsadda, Pakistan for the study leave for his doctoral studies. L. Yuan thanks the financial support of Natural Science Foundation of China (Grant Nos. 91852116, 12071470, 12161141017).

### References

- [1] Kelvin L. Hydrokinetic solutions and observations. *Phil Mag* 1871;42:362–77.
- [2] Helmholtz H. On discontinuous movements of fluids. *Phil Mag* 1868;36:337–46.
- [3] Taylor GI. Effect of variation in density on the stability of superposed streams of fluid. *Proc R Soc Lond Ser A Math Phys Eng Sci* 1931;132:499–523.
- [4] Thorpe SA. A method of producing a shear flow in a stratified fluid. *J Fluid Mech* 1968;32:693–704.
- [5] Hazel P. Numerical studies of the stability of inviscid stratified shear flows. *J Fluid Mech* 1972;51:39–61.

- [6] Fakhari A, Lee T. Multiple-relaxation-time lattice Boltzmann method for immiscible fluids at high Reynolds numbers. *Phys Rev E* 2013;87:023304.
- [7] Chen MJ, Forbes LK. Accurate methods for computing inviscid and viscous kelvin–Helmholtz instability. *J Comput Phys* 2011;230:1499–515.
- [8] Lee HG, Kim J. Two-dimensional Kelvin–Helmholtz instabilities of multi-component fluids. *Eur J Mech B Fluids* 2015;49:77–88.
- [9] Funada T, Joseph DD. Viscous potential flow analysis of Kelvin–Helmholtz instability in a channel. *J Fluid Mech* 2001;445:263–83.
- [10] Funada T, Joseph DD. Viscous potential flow analysis of capillary instability. *Int J Multiph Flow* 2002;28:1459–78.
- [11] Joseph DD, Wang J. The dissipation approximation and viscous potential flow. *J Fluid Mech* 2004;505:365–77.
- [12] Awasthi MK, Asthana R, Agrawal GS. Viscous correction for the viscous potential flow analysis of Kelvin–Helmholtz instability of cylindrical flow with heat and mass transfer. *Int J Heat Mass Transfer* 2014;78:251–9.
- [13] Shadloo MS, Yildiz M. Numerical modeling of Kelvin–Helmholtz instability using smoothed particle hydrodynamics. *Internat J Numer Methods Engrg* 2011;87:988–1006.
- [14] Zhang R, He X, Doolen G, Chen S. Surface tension effects on two-dimensional two-phase kelvin–Helmholtz instabilities. *Adv Water Resour* 2001;24:461–78.
- [15] Atmakidis T, Kenig EY. A study on the Kelvin–Helmholtz instability using two different computational fluid dynamics methods. *J Comput Multiph Flows* 2010;2:33–45.
- [16] Shin S, Sohn S, Hwang W. Vortex simulations of the Kelvin–Helmholtz instability with surface tension in density-stratified flows. *Eur J Mech B Fluids* 2018;67:168–77.
- [17] Sohn S, Yoon D, Hwang W. Long-time simulations of the Kelvin–Helmholtz instability using an adaptive vortex method. *Phys Rev E* 2010;82:046711.
- [18] Tauber W, Unverdi SO, Tryggvason G. The nonlinear behavior of a sheared immiscible fluid interface. *Phys Fluids* 2002;14:2871–85.
- [19] Rangel RH, Sirignano WA. Nonlinear growth of Kelvin–Helmholtz instability: effect of surface tension and density ratio. *Phys Fluids* 1988;31:1845–55.
- [20] Redapangu PR, Sahu KC, Vanka SP. A study of pressure-driven displacement flow of two immiscible liquids using a multiphase lattice Boltzmann approach. *Phys Fluids* 2012;24:102110.
- [21] Redapangu PR, Sahu KC, Vanka SP. A lattice Boltzmann simulation of three dimensional displacement flow of two immiscible liquids in a square duct. *J Fluids Eng* 2013;135:121202.
- [22] Cenicerros HD, Roma AM. Study of the long-time dynamics of a viscous vortex sheet with a fully adaptive nonstiff method. *Phys Fluids* 2004;16:4285–318.
- [23] Sohaib M, Shah A. Fully decoupled pressure projection scheme for the numerical solution of diffuse interface model of two-phase flow. *Commun Nonlinear Sci Numer Simul* 2022;112:106547.
- [24] Chorin AJ. A numerical method for solving incompressible viscous flow problems, 2 (1967) 12–26.
- [25] Breuer M, Hanel D. A dual time-stepping method for 3-d, viscous, incompressible vortex flows. *Comput & Fluids* 1993;22:467–84.
- [26] Shu CW. Essentially non-oscillatory and weighted essentially non-oscillatory schemes for hyperbolic conservation laws. In: Quarteroni A, editor. *Advanced numerical approximation of nonlinear hyperbolic equations. lecture notes in mathematics*, Vol 1697. Berlin, Heidelberg: Springer; 1998. <http://dx.doi.org/10.1007/BFb0096355>.
- [27] Khan SA, Shah A, Saeed S. Numerical simulation of the interaction between three equal-sized rising bubbles using the phase-field method. *AIP Adv* 2020;10:055218.
- [28] Shah A, Yuan L. Numerical solution of a phase-field model for incompressible two-phase flows based on artificial compressibility. *Comput & Fluids* 2011;42:54–61.
- [29] Borges RL, Carmona M, Costa B, Don WS. An improved weighted essentially non-oscillatory scheme for hyperbolic conservation laws. *J Comput Phys* 2008;227:3191–211.
- [30] Soh WY, Goodrich JW. Unsteady solution of incompressible Navier–Stokes equations. *J Comput Phys* 1988;79:79, 113–134.
- [31] Ramshaw JD, Mousseau VA. Accelerated artificial compressibility method for steady-state incompressible flow calculations. *Comput & Fluids* 1990;18:361–7.
- [32] Turkel E, Armone A. Pseudo-compressibility methods for the incompressible flow equations. *ICASE Report* 93-66, 1993.
- [33] Kwak D, Chang JLC, Shanks SP, Chakravarthy SR. A three-dimensional incompressible Navier–Stokes flow solver using primitive variables. *AIAA J* 1986;24:390–6.
- [34] Rogers SE, Kwak D. An upwind differencing scheme for the time-accurate incompressible Navier–Stokes equations. *AIAA J* 1990;28(2):253–62.